

## Green Bank Telescope Discovery of the Redback Binary Millisecond Pulsar PSR J0212+5321

KAREN I. PEREZ <sup>1</sup>, SLAVKO BOGDANOV <sup>2</sup>, JULES P. HALPERN <sup>1,2</sup> AND VISHAL GAJJAR <sup>3</sup>

<sup>1</sup>*Department of Astronomy, Columbia University, 550 West 120th Street, New York, NY 10027, USA*

<sup>2</sup>*Columbia Astrophysics Laboratory, Columbia University, 550 West 120th Street, New York, NY 10027, USA*

<sup>3</sup>*Department of Astronomy, University of California Berkeley, Berkeley CA 94720*

(Accepted June 9, 2023)

Submitted to ApJ

### ABSTRACT

We report the discovery of a 2.11 ms binary millisecond pulsar during a targeted search of the redback optical candidate coincident with the  $\gamma$ -ray source 3FGL J0212.5+5320 using the Robert C. Byrd Green Bank Telescope (GBT) with the Breakthrough Listen backend at L-band. Over a seven month period, five pointings were made near inferior conjunction of the pulsar in its 20.9 hr orbit, resulting in two detections, lasting 12 and 42 minutes. The pulsar dispersion measure (DM) of  $25.7 \text{ pc cm}^{-3}$  corresponds to a distance of 1.15 kpc in the NE2001 Galactic electron density model, consistent with the Gaia parallax distance of  $1.16 \pm 0.03$  kpc for the companion star. We suspect the pulsar experiences wide-orbit eclipses, similar to other redbacks, as well as scintillation and DM delays caused by its interaction with its companion and surroundings. Although the pulsar was only detected over  $\approx 3.7\%$  of the orbit, its measured acceleration is consistent with published binary parameters from optical radial velocity spectroscopy and light-curve modeling of the companion star, and it provides a more precise mass ratio and a projected semi-major axis for the pulsar orbit. We also obtained a refined optical photometric orbit ephemeris, and observed variability of the tidally distorted companion over 7 years. A hard X-ray light curve from NuSTAR shows expected orbit-modulated emission from the intrabinary shock. The pulsar parameters and photometric ephemeris greatly restrict the parameter space required to search for a coherent timing solution including pulsar spin-down rate, either using Fermi  $\gamma$ -rays, or further radio pulse detections.

*Keywords:* Pulsars; Millisecond Pulsars; Redbacks

### 1. INTRODUCTION

Compared to the population of ordinary pulsars, millisecond pulsars (MSPs) have much shorter spin periods ( $P_s \lesssim 30$  ms), smaller spin-down rates ( $\dot{P}_s \sim 10^{-22} - 10^{-17}$  s/s), weak magnetic fields ( $B_s \sim 10^7 - 10^{11}$ ), and long spin-down timescales of  $\tau \sim 10^9 - 10^{10}$  years (Hui & Li 2019). Since their discovery by Backer et al. (1982), it has been commonly accepted that MSPs have been recycled by the transfer of matter and angular momentum from a companion star during an X-ray binary phase (Alpar et al. 1982). This has been supported by the discovery of three transitional millisecond pulsars (tMSPs). They are characterized by instantaneous switches between two clearly distinguishable states: an accreting low-mass X-ray binary (LMXB) and a rotationally-

powered MSP – both of which last for several years in a single instance (Archibald et al. 2009; Papitto et al. 2013; Bassa et al. 2014; Stappers et al. 2014). This interaction is due to the balance between the outward pressure exerted by the pulsar wind on the mass lost by its companion, and the inward pull applied by the gravitational field of the pulsar (Bhattacharya & van den Heuvel 1991; Papitto & de Martino 2020). While the more common MSP binaries have white dwarf companions and wide orbits ( $P_b > 1$  day), the interacting MSP systems have a low-mass stellar or sub-stellar companion, and orbits that have been circularized through tidal interactions, with  $P_b < 1$  day (Fruchter et al. 1988; Roberts 2013). Black widows have degenerate companions with  $M_2 < 0.05 M_\odot$ , while redbacks have hydrogen-rich, non-degenerate companions (Roche-lobe filling or nearly so) with  $0.1 M_\odot \lesssim M_2 \lesssim 1 M_\odot$  (Strader et al. 2019). Deriving their names from spider species which prey on their mates, pulsars in these binary systems ab-

late their companions and possibly destroy some completely to become isolated MSPs.

Redbacks are a growing class of binary MSPs. Originally discovered in globular clusters (Camilo et al. 2000; Edmonds et al. 2002; D’Amico et al. 2001b; Ransom et al. 2005), there are currently over two dozen such systems known in the field of the Galaxy, either confirmed or candidate (Roberts 2013; Bogdanov et al. 2021), demonstrating that they are not exclusive to globular clusters as initially thought. The discovery of tMSPs has been key to investigating the evolution of MSPs, as we work towards understanding whether they are solely an intermediate step before they end as radio pulsars devouring their companions, or are instead a road to a different evolutionary path.

The radio eclipse properties of redback systems are highly variable, and they are strongly frequency dependent, with generally much longer eclipses at lower frequencies. In addition, at lower frequencies, random, brief eclipses are observed at all phases (Archibald et al. 2009). Such eclipses and dispersion measure variations are attributed to the presence of gas flowing out from the companion due to irradiation by the pulsar wind.

Redbacks are detected with surprising frequency in high-energy  $\gamma$ -rays by the Fermi Large Area Telescope (LAT), and are identified as such by follow-up radio pulsar searches of Fermi unassociated  $\gamma$ -ray sources. A number of Fermi LAT sources have been found to contain optical and X-ray counterparts with properties virtually identical to those of confirmed redback MSPs, but no radio pulsations have been found so far. In many cases, redback MSPs are discovered in the radio only after several observations of the source. Multiple observations increase the chances that an intermittently detectable pulsar will be glimpsed despite the interstellar scintillation, large acceleration at an unfavorable binary phase, or eclipses caused by the material emanating from the companion star.

In this paper, we present the discovery of the redback binary MSP PSR J0212+5321, along with optical and X-ray observations of the 3FGL J0212.1+5320 system. In Section 2 we summarize the  $\gamma$ -ray, optical, and X-ray properties indicating 3FGL J0212.1+5320 to be a redback MSP. In Section 3 we outline our observations and observing strategy with the Green Bank Telescope (GBT) at L-band, and detail our search, analysis, and discovery in Section 4. Section 5 describes our optical monitoring observations and refined optical ephemeris using the MDM Observatory and the Zwicky Transient Facility (ZTF). Section 6 covers X-ray monitoring observations with the Nuclear Spectroscopic Telescope Array (NuSTAR), Swift, and Chandra. We discuss the implications of our findings and derived parameters in Section 7, and Section 8 lists our final conclusions.

## 2. HISTORY OF 3FGL J0212.1+5320

The high-energy  $\gamma$ -ray source 3FGL J0212.1+5320 (presently cataloged as 4FGL J0212.1+5321) first appeared in the initial Fermi LAT source catalog (Abdo et al. 2010). It was deemed to be a strong MSP candidate through the use of statistical and machine-learning techniques (Saz Parkinson et al. 2016; Mirabal et al. 2016). Linares et al. (2017) found 3FGL J0212.1+5320 to have a low variability and a curved  $\gamma$ -ray spectral shape, both  $\gamma$ -ray properties of pulsars from the *Fermi* LAT catalog (Abdo et al. 2013).

Follow-up photometry and optical spectroscopy by Li et al. (2016) and Linares et al. (2017) found a variable optical and X-ray counterpart to the source – a nearby ( $\approx 1.1$  kpc) binary system with a 20.9 hour period and an optically bright ( $r' \approx 14.3$  mag) tidally deformed main-sequence secondary star of spectral type  $\approx$  F6 and mass  $\approx 0.4 M_{\odot}$ , making it the brightest in the optical band out of all known redbacks (confirmed and candidates). Li et al. (2016) determined an orbital period  $P_b = 0.869575(4)$  days, which we further refine in this paper. Linares et al. (2017) found that its optical lightcurve was similar to those observed in the confirmed redback MSPs PSR J1628–3205 ( $P_b = 5.0$  hr; Li et al. 2014) and PSR J2129–0429 ( $P_b = 15.2$  hr; Bellm et al. 2016). Detailed modeling of the optical light curve by Shahbaz et al. (2017), including heating or starspot effects, put further constraints on the binary parameters such as mass ratio and inclination angle.

The X-ray-to- $\gamma$ -ray flux ratio and  $\gamma$ -ray luminosity of  $L_{\gamma} = 2.5 \times 10^{33}$  erg s $^{-1}$  are also typical of MSPs. *Chandra* X-ray observations revealed a power-law spectrum with  $\Gamma \approx 1.3$  and luminosity of  $L_X = 2.6 \times 10^{32}$  erg s $^{-1}$ , consistent with the presence of a synchrotron-emitting intrabinary shock and making it the brightest non-accreting redback candidate in the X-rays.

## 3. STRATEGY AND GBT OBSERVATIONS

We observed the optical/X-ray candidate for 3FGL J0212.1+5320 at L-band (central frequency of  $\nu_c = 1501$  MHz) on five dates between 2022 February 11 and 2022 September 5 with the GBT using the Breakthrough Listen Digital Backend (BLDB; MacMahon et al. 2018) to conduct a deep search for radio pulsations and confirm its identification as a binary MSP. We opted for the L-band frequency range because it is advantageous to observe at the highest frequency feasible, as eclipses tend to last longer at lower frequencies. On the other hand, L-band is an adequate compromise for MSPs, which generally have relatively steep radio spectra indices, ranging from approximately  $-3$  to  $-1.5$  (Frail et al. 2016).

Our observations covered 1.3–1.85 GHz, with an effective bandwidth of 550 MHz. We collected baseband voltages and converted them to high-time resolution total intensity filterbank products. The number of observing channels was 16,384, with a channel bandwidth of 91 kHz, and a sampling time of 43  $\mu$ s. A detailed summary

of the BL reduction pipeline and discussion of various data products is provided by [Lebofsky et al. \(2019\)](#).

A summary of all our on-source observations, including observation lengths and corresponding orbital phases, is given in Table 1. We observed the binary at around pulsar inferior conjunction (orbital phase  $\phi = 0.75$ ), when the pulsar is between the companion and the observer, to minimize the chance of eclipses. We computed the orbital phase using a refined optical photometric ephemeris obtained at the MDM Observatory; this is further discussed in Section 5.2. Observations were separated by at least a month to mitigate against possible changes in eclipse duration on timescales of weeks/months, as seen in observations of redbacks such as PSR J1048+2339 ([Deneva et al. 2016](#)). Our detections are listed in Table 2, and will be discussed further below.

## 4. GBT DATA ANALYSIS AND RESULTS

### 4.1. Pulse Search and Discovery

All observations were processed and searched for pulsars using standard PRESTO<sup>1</sup> routines ([Ransom 2001](#)). Radio frequency interference (RFI) masks were created for each observation using `rfifind`. We used the RFI mask with `prepsubband` to generate de-dispersed time series across 0–60 pc cm<sup>-3</sup>, with a DM step of 0.1 pc cm<sup>-3</sup> without any restrictions on the spin period. When generating these time series, we fixed the pulsar position at the Gaia Data Release 3 (DR3) coordinates including proper motion ([Gaia Collaboration et al. 2016, 2022](#)) as listed in Table 3, and corrected the times to the solar system barycenter. We then Fourier transformed the time series with `realfft`. The resulting power spectra were summed up to the eighth harmonic and a Fourier-domain acceleration search was performed to search for periodic signals using `accelsearch` with  $z_{\max} = 200$ , where  $z_{\max}$  indicates the largest number of Fourier bins by which a pulse is allowed to smear across frequency. We do not conduct jerk searches (for changing acceleration), as J0212+5321 is not highly accelerated, and sensitivity would only improve for observation lengths  $T_{\text{obs}} \sim 0.05 - 0.15 P_b$  ([Andersen & Ransom 2018](#)), corresponding to 1–3 hr long observations for this orbital period. Using the `sifting` script, candidates without duplicates or DM problems were folded with `prepfold` for visual inspection, where the number of sampling bins was automatically selected based on the period.

The main candidate was found in the full Obs 03 integration from 2022 April 19 at a period of 2.11 ms and DM of 25.7 pc cm<sup>-3</sup>, using 48 sampling bins. Its detection parameters are listed in Table 2. Shown in Figure 1a, the signal was seen for the first  $\approx 720$  seconds, corresponding to orbital phases 0.706–0.716, just before

pulsar inferior conjunction. Using the effective bandwidth, Figure 2a shows the frequencies at which PSR J0212+5321 was detected. The pulsar dominates the top-half of the band from  $\sim 1500 - 1800$  MHz, indicating a low-frequency cutoff  $\sim 1500$  MHz.

We folded the raw data for all other observations at the identified period and DM, at both the full- and sub-integrations of the observations (considering the possibility of brief eclipses), as noted in Table 1. For observations longer than 10 minutes, the full observation was split into sub-integrations according to its length. Obs 02, 04, and 05 were divided into eight sub-integrations, while Obs 03 was divided into four. Given the Doppler effect on detection parameters, we additionally ensured a thorough search by folding each full observation and its sub-integrations at a range of spin periods and derivatives for a circular orbit, given their respective phases and accounting for systematic errors (see Section 7.1 for more details). We allowed for both a search in DM space, and a targeted search at the previously detected DM of 25.7 pc cm<sup>-3</sup>.

While we did not detect the pulsar in Obs 01, 02, and 04, observations conducted on 2022 September 5 (Obs 05) resulted in a second detection of PSR J0212+5321, with similar detection parameters as listed in Table 2. As shown in Figure 1b, similar to Obs 03, the pulsar is visible through almost the entire session of Obs 05,  $\approx 42$  min out of 46 min, corresponding to orbital phases 0.698–0.732, with occasional dimming most likely due to intrabinary material surrounding the pulsar. Unlike Obs 03, Figure 2b shows the pulsar much dimmer at mid- and lower-frequencies, peaking in intensity from  $\sim 1790 - 1850$  MHz. This leads us to believe the pulsar might be easily detectable at higher frequencies, e.g., S-band (2–4 GHz), or else the narrow-band excess could be a manifestation of interstellar scintillation.

For Obs 05, we strategically chose to observe the pulsar at orbital phases closer to that of Obs 03, in case there is persistent visibility confined to phases preceding pulsar inferior conjunction. However, we cannot yet conclude that these two detections were strictly determined by orbital phase rather than random variability (see Section 7.2 for a discussion).

### 4.2. Sensitivity and Flux Density

A test pulsar, PSR B0329+54, was observed for 5 minutes prior to every observing session to verify our equipment sensitivity. We recovered it during all five of our observations with blind PRESTO searches at  $z_{\max}=0$ . We also detected harmonics of the slow 376 ms pulsar, PSR J0212+5222 ([Barr et al. 2013](#); [Lynch 2012](#)), at its known DM of 38.2 pc cm<sup>-3</sup> in the side-lobes of the telescope for all five observations.

While our observations were not flux-calibrated, here we estimate our pulsar sensitivity using standard methods. Using `dspsr`'s `pdmp` to optimize the S/N of the pulse profile, we compute the flux density for each

<sup>1</sup> Available for download from <https://github.com/scottransom/presto>.

**Table 1.** Log of GBT Observations of 3FGL J0212.1+5320

Obs	Date (UT)	Start/Stop Time (UTC)	Start/Stop Time (BMJD TDB)	Orbital Phase <sup>a</sup> ( $\phi$ )	Total Exposure (min)	Sub-integration <sup>b</sup> (min)
01	2022-02-11	04:22:39 – 04:30:26	59621.18309 – 59621.18850	0.769 – 0.775	7.8	7.8
02	2022-03-10/11	23:48:38 – 00:30:02	59648.99068 – 59649.01942	0.748 – 0.781	41.4	5.175
03	2022-04-19	23:00:38 – 23:15:23	59688.95527 – 59688.96551	0.706 – 0.718	14.7	3.675
04	2022-05-24	18:27:01 – 19:15:20	59723.76500 – 59723.79856	0.737 – 0.776	48.3	6.0375
05	2022-09-05	04:59:39 – 05:45:39	59827.21055 – 59827.24250	0.698 – 0.735	46.01	5.75

<sup>a</sup>Predicted from the optical photometric ephemeris (Section 5.2).

<sup>b</sup>The length the observation was equally split into to thoroughly search for the pulsar.

**Table 2.** PRESTO Parameters of PSR J0212+5321 Detections with the GBT

Obs	DM (pc cm <sup>-3</sup> )	$T_{\text{epoch}}$ (BMJD TDB)	$P_s^a$ (ms)	$\dot{P}_s^a$ (s s <sup>-1</sup> )	Significance <sup>b</sup> ( $\sigma$ )
03	25.68	59688.95527	2.11459814(16)	$2.99(14) \times 10^{-11}$	14.6
05	25.72	59827.21055	2.114580210(38)	$2.987(11) \times 10^{-11}$	23.9

<sup>a</sup>Apparent spin period and period derivative at  $T_{\text{epoch}}$ .

<sup>b</sup>Equivalent Gaussian significance, based on the probability of seeing a noise value with the same incoherently summed power (Ransom et al. 2002).

of the two observations using the radiometer equation (Lorimer & Kramer 2004)

$$S_{1500} = \frac{S/N T_{\text{sys}}}{G \sqrt{n_p \Delta\nu T_{\text{obs}}}} \sqrt{\frac{W_{50}}{P_s - W_{50}}}, \quad (1)$$

where  $S/N$  is the signal-to-noise ratio of PSR J0212+5321,  $T_{\text{sys}}$  is the equivalent temperature of the system (receiver, spillover, and sky),  $n_p$  is the number of polarizations,  $G$  is the telescope gain, and  $\Delta\nu$  is the effective bandwidth.  $T_{\text{obs}}$  is the integration time, and  $W_{50}$  and  $P_s$  are the absolute pulse width and apparent spin period, respectively. We use  $n_p = 2$ ,  $G = 2.0$  K Jy<sup>-1</sup>,  $T_{\text{sys}} = 17.1$  K, and  $\Delta\nu = 550$  MHz. We use an S/N of 16.66 and 27.29, and a  $W_{50}$  of 0.132 ms and 0.176 ms, for Obs 03 and 05, respectively. We derive a flux density,  $S_{1500}$  of 0.037 mJy and 0.040 mJy for Obs 03 and 05, respectively. Using the Gaia-derived distance, this corresponds to a radio luminosity,  $L_{1500}$  of 0.05 mJy kpc<sup>2</sup>. We report the pulsar parameters measured with Obs 05 in Table 3.

#### 4.3. Distance

Gaia’s DR3 parallax for PSR J0212+5321 corresponds to a distance of  $1.16 \pm 0.03$  kpc. We also estimate the

distance using two Galactic electron density distribution models from Price et al. (2021)’s PyGEDM. Using the DM of 25.7 pc cm<sup>-3</sup> at Galactic coordinates of  $l = 134^\circ.92$ ,  $b = -7^\circ.62$ , the NE2001 (Cordes & Lazio 2002, 2003) model predicts  $d_{\text{NE2001}} = 1.15$  kpc, while the YMW16 (Yao et al. 2017) model predicts  $d_{\text{YMW16}} = 1.27$  kpc. The NE2001 model is most consistent with Gaia.

#### 4.4. Timing Anomaly

During Obs 05, there is a timing anomaly near the beginning (Figure 1b) lasting for  $\approx 400$  s during which the pulse is delayed by  $\approx 0.1 P_s$ . The cause could be transient extra plasma in the system with electron column  $\delta\text{DM} \approx 0.13$  pc cm<sup>-3</sup> (using an average frequency of 1600 MHz). If originating in a spherical clump transiting the line of sight with the relative velocity of the stars ( $\approx 275$  km s<sup>-1</sup>), it would have an electron density of  $\approx 3.7 \times 10^7$  cm<sup>-3</sup> (see Section 7.2 for further discussion).

### 5. OPTICAL TIME-SERIES MONITORING

We collected optical time-series of 3FGL J0212.1+5320 from 2016 to 2023 in order to monitor for variability, and to extend its orbital ephemeris for use in conjunction with the pulsar search. The

**Table 3.** Parameters of PSR J0212+5321

Parameter	Value
R.A. (Gaia-CRF3) <sup>a</sup> , $\alpha$	02 <sup>h</sup> 12 <sup>m</sup> 10 <sup>s</sup> .47274
Decl. (Gaia-CRF3) <sup>a</sup> , $\delta$	53°21′38″.8110
Epoch of position <sup>a</sup>	2016.0
Proper motion <sup>a</sup> in R.A., $\mu_\alpha \cos \delta$ (mas yr <sup>-1</sup> )	-2.627(23)
Proper motion <sup>a</sup> in decl., $\mu_\delta$ (mas yr <sup>-1</sup> )	+2.044(21)
Parallax distance <sup>a</sup> , $d$ (kpc)	1.16(03)
Epoch of pulsar ascending node at $\phi = 0^b$ , $T_0$ (BMJD TDB)	58487.45679(86)
Orbital period <sup>b</sup> , $P_b$ (days)	0.8695759(11)
Intrinsic spin period <sup>c</sup> , $P_{s,0}$ (ms)	2.1147(1)
Mass ratio <sup>d</sup> , $q = M_2/M_1$	0.2469 ± 0.0067 ± 0.010
Projected semi-major axis <sup>d</sup> , $(a_1/c) \sin i$ (lt-s)	2.132 ± 0.008 ± 0.09
Dispersion Measure <sup>e</sup> , DM (pc cm <sup>-3</sup> )	25.7
DM distance based on NE2001, $d_{NE2001}$ (kpc)	1.15
DM distance based on YMW16, $d_{YMW16}$ (kpc)	1.27
1500 MHz flux density <sup>e</sup> , $S_{1500}$ (mJy)	0.04
1500 MHz radio luminosity <sup>e</sup> , $L_{1500} = S_{1500} d^2$ (mJy kpc <sup>2</sup> )	0.05
Pulse width <sup>e</sup> at 1500 MHz, $W_{50}$ (ms)	0.176

<sup>a</sup>From Gaia DR3 (Gaia Collaboration et al. 2022).

<sup>b</sup>From the MDM optical photometric ephemeris (Section 5.2).

<sup>c</sup>Derived in Section 7.1. Uncertainty is dominated by possible systematic error in orbital phase.

<sup>d</sup>Derived in Section 7.1. The second uncertainty represents possible systematic error in orbital phase.

<sup>e</sup>Measured from GBT Obs 05.

data were obtained with the MDM Observatory 1.3 m McGraw-Hill telescope in the  $V$  band at 63 s cadence, and were reduced using differential photometry with respect to a nearby comparison star. Figure 3 shows the light curves from the 39 nights, in time order from panels (a) through (k), folded on the orbital ephemeris (see Section 5.2).

We also used the 16th data release from the ZTF (Masci et al. 2018; Bellm et al. 2019), which provided 1541 good exposures in  $r$  and 907 in  $g$  over the years 2018–2022. Figure 4 shows the ZTF points grouped into the five observing seasons. The most recent season (2022–2023) is not yet complete.

### 5.1. Light Curve Variability

Dominated by ellipsoidal modulation, the light curves of 3FGL J0212.1+5320 also reveal significant variability on time scales of months. In each panel of Figure 3, data exhibiting consistent states are grouped together. While a detailed heating model was applied by Shahbaz

et al. (2017) to the original light curves of Linares et al. (2017), it is now apparent that different results would necessarily be obtained at other epochs. The now familiar variability of redback companion light curves (Bellm et al. 2016; van Staden & Antoniadis 2016; Li et al. 2014; Cho et al. 2018; Clark et al. 2020; Halpern et al. 2022) can be attributed to one or more causes: changing Roche-lobe filling factor, starspots, variable photospheric heating by the intrabinary shock, and/or heating by the magnetically ducted pulsar wind.

Although detailed modeling of these light curves is beyond the scope of this work, it is meaningful to use the basic parameters of the system that were fitted by Shahbaz et al. (2017), including mass ratio, inclination angle, and Roche-lobe filling factor, but neglecting pulsar heating and hot or cold spots, to examine how our data would compare to a model of pure ellipsoidal modulation. For this purpose we used the fitted orbital parameters from the hot-spot model of Shahbaz et al. (2017),  $q = M_2/M_1 = 0.28$ ,  $i = 69^\circ$ , and volume filling fac-

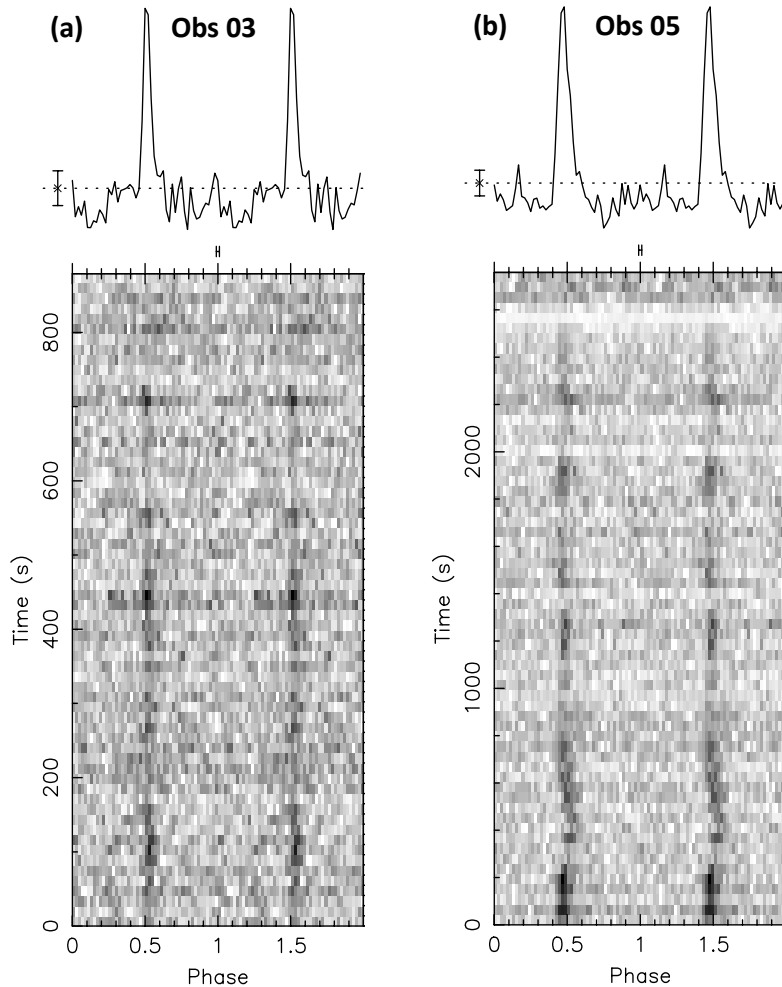


**Figure 1.** Time-resolved radio detections of PSR J0212+5321 taken at 1500 MHz with the GBT from (a) 2022 April 19 and (b) September 5, respectively. The length of the observations are 14.7 and 46 minutes, respectively. The folded pulse profiles are shown twice as a function of time and summed at the top.

tor  $f = 0.76$ , to produce a purely ellipsoidal curve using the analytic approximations of [Morris & Naftilan \(1993\)](#) and [Gomel et al. \(2021\)](#). For compatibility with the analytic model, we used a linear limb-darkening coefficient  $u = 0.6$  appropriate for the F6 spectral type ([Claret & Bloemen 2011](#)). The red curve in Figure 3 represents this model. The data in Figure 3g conforms to the model very well, so we normalized the model there. At this epoch the star was in its faintest state, with a minimum of the light curve at  $V = 14.60$ .

Notably, the magnitudes from [Linares et al. \(2017\)](#) to which [Shahbaz et al. \(2017\)](#) fit their model also correspond closely to our data in Figure 3g. Their light-curve minima at  $r' = 14.38$  and  $g' = 14.97$  transform to  $V = 14.62$ , very close to our  $V = 14.60$ . Data in the other panels show varying degrees of departure from the model, mostly lying above it (by up to 0.1 mag), and including deviations from pure ellipsoidal effects such as those mentioned above and reviewed in [Halpern et al. \(2022\)](#). Note that the Roche-lobe filling factor, mod-

elled as 0.76 in volume or 0.91 in radius, could increase without leading to overflowing and mass transfer.

The ZTF light curves in Figure 4 reinforce the evidence for long-term variability that is sparsely sampled by the MDM data. The brightness appeared to reach a minimum in 2019–2020, just as in the MDM data, while the star was brighter in 2017–2018, and was again near maximum in 2021–2022. In addition, within individual observing seasons, several of the ZTF light curves show excess variance around the mean ellipsoidal shape, which is indicative of variability on shorter timescales, again confirming such evidence from the MDM runs.

## 5.2. New Orbital Ephemeris

We used the MDM data to obtain a photometric orbital ephemeris that extends and refines the original ones from [Li et al. \(2016\)](#) and [Linares et al. \(2017\)](#). The 21 hr orbit does not allow complete phase coverage during a typical observing run. This, plus the obvious long-term variability of the light curve, is not conducive to tem-

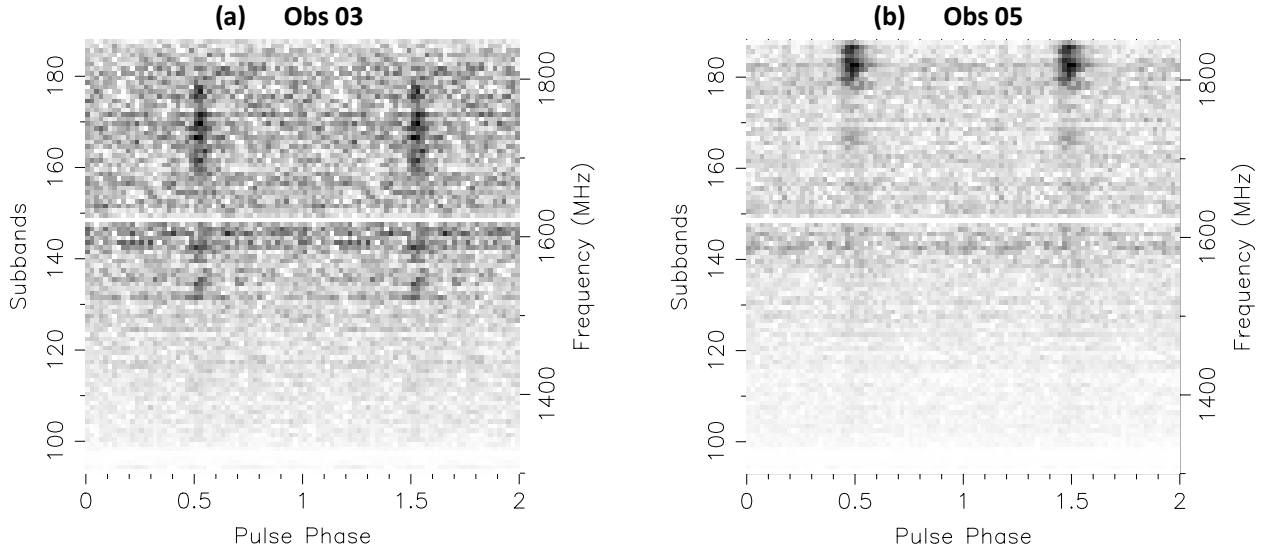


**Figure 2.** Sub-band plot for Obs 03 and 05, respectively, where 48 profile bins were used and each sub-band is 5.86 MHz wide for a total of 256 sub-bands. For data clarity, only sub-bands corresponding to frequencies 1.3–1.85 GHz (sub-bands 93–188) are shown.

plate fitting as a method of timing. Instead we make use of those segments that include a well covered extremum of the light curve, either maximum or minimum, to use as fiducial markers of orbital phase. Phase 0 is the presumed ascending node of the pulsar, corresponding to a maximum of the light curve due to the projection of the tidally distorted companion star. The first minimum, at phase 0.25, is the presumed inferior conjunction of the companion, and so on.

We found a total of 26 useful timings of the extrema between 2017 and 2023, and supplemented these with two useful timings in  $r$  and  $i$  filters during 2015 December from Linares et al. (2017). Fitting these 28 timings to a constant period leaves residuals of  $< 0.01$  cycles, with only small systematic deviations from ellipsoidal symmetry. The fitted orbital period is  $P_b = 0.8695759(11)$  day, with  $T_0 = 58,487.45679(86)$  BMJD as the epoch of phase 0. The span of the observations is MJD 57,378–59,971.

Random variability of the light curve shape may account for the bulk of the error bars on the ephemeris parameters. Also, several panels in Figure 3 show timing variations of the maximum and minimum of up to  $\approx 0.03$  cycles. This suggests that  $T_0$  is not as precise as its fitted formal uncertainty. Since  $T_0$  is a photometric quantity and not a kinematic measurement, it can be expected to deviate from the true time of ascending node of the pulsar by an unknown systematic error much larger than its statistical uncertainty. See Section 7.1 for further discussion of this.

We also fitted for the orbital period in the ZTF data using a Lomb-Scargle periodogram. The value of the first harmonic, which contains more power than the fundamental, was adopted. The resulting  $P_b$  is 0.869566(7)

day and 0.869575(8) day for the  $r$  and  $g$  points, respectively. These are both consistent with the contemporaneous MDM value, but not as precise. Therefore, we simply folded the ZTF data in Figure 4 on the MDM ephemeris.

## 6. X-RAY OBSERVATIONS

The field around 3FGL J0212.1+5320 has been covered by multiple X-ray telescopes including NuSTAR, Swift, and Chandra. All X-ray observations of 3FGL J0212.1+5320 presented here are summarized in Table 4 of the Appendix. Swift UVOT magnitudes are listed in Table 5.

### 6.1. NuSTAR

The 3FGL J0212.1+5320 system was observed with the Nuclear Spectroscopic Telescope Array (NuSTAR; Harrison et al. 2013) on 2020 October 5–7 (ObsID 30601011) in a 81.7 ks deadtime-corrected on-source exposure. The total elapsed time of the observation was 168.4 ks, which covers 2.2 consecutive orbital cycles of the 3FGL J0212.1+5320 binary. The event data were processed using the `nupipeline` script in NuSTAR-DAS and the images, spectra, and barycentered and background-subtracted light curves were generated using the `nuproducts` task. 3FGL J0212.1+5320 is the only hard X-ray source within the NuSTAR field of view and is detected above the background level up to  $\sim 30$  keV. For both the spectroscopic and time-variability analyses, the source counts were extracted from a circular region of radius  $60''$  (which encircles  $\sim 80\%$  of the total energy of the point spread function) centered on the Gaia optical position.

The background-subtracted NuSTAR light curve, with events from Focal Plane Modules A and B (FPMA

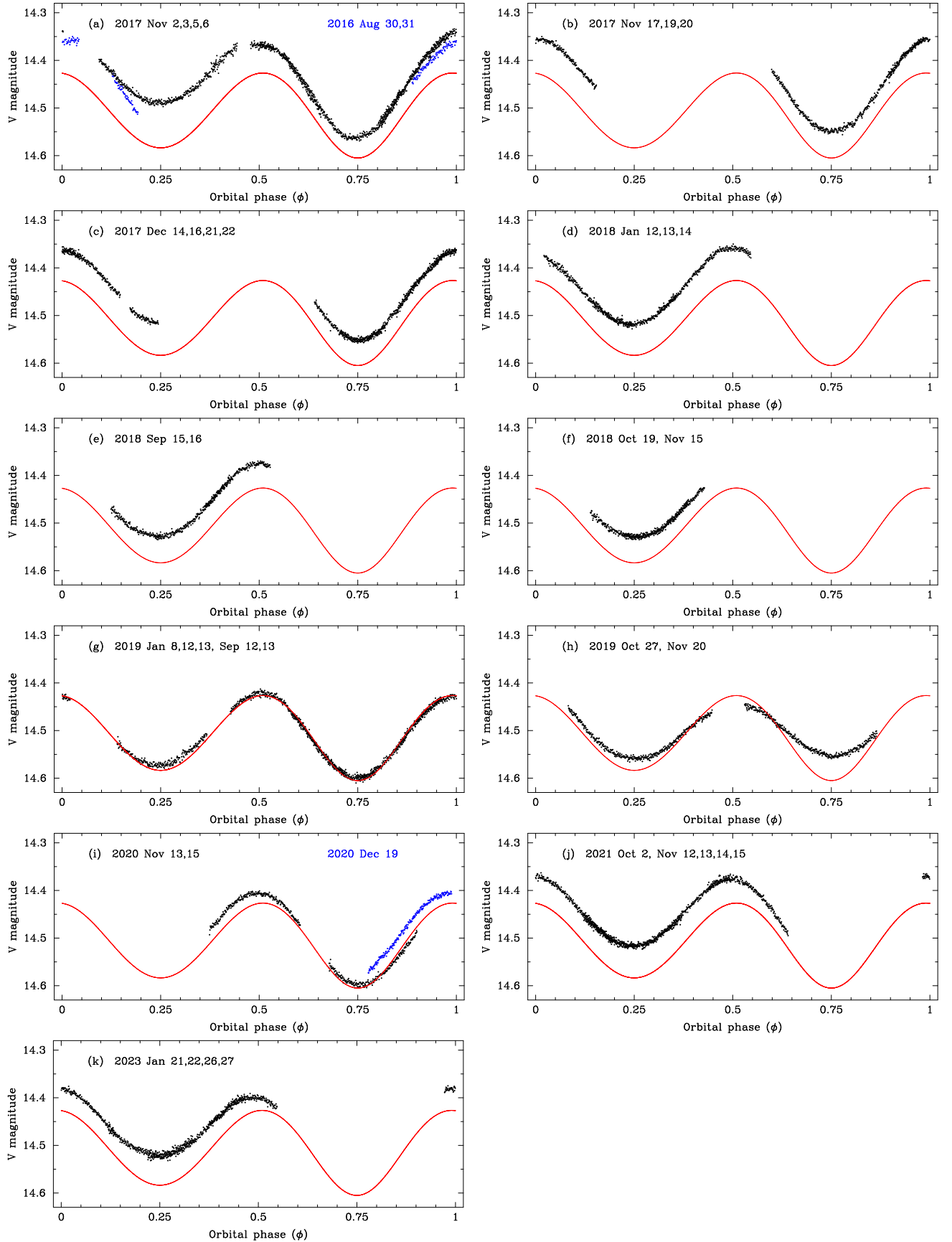


**Figure 3.** V-band time-series photometry of 3FGL J0212.1+5320 from the MDM 1.3 m, folded according to the orbital ephemeris calculated from these data (see Section 5.2). Dates are given in each panel. The red curve is a pure ellipsoidal model (Morris & Naftilan 1993; Gomel et al. 2021) using the fitted orbital parameters (mass ratio, inclination angle, and Roche-lobe filling factor) from Shahbaz et al. (2017). It is normalized to the data in panel (g), but is otherwise not a fit to the data.



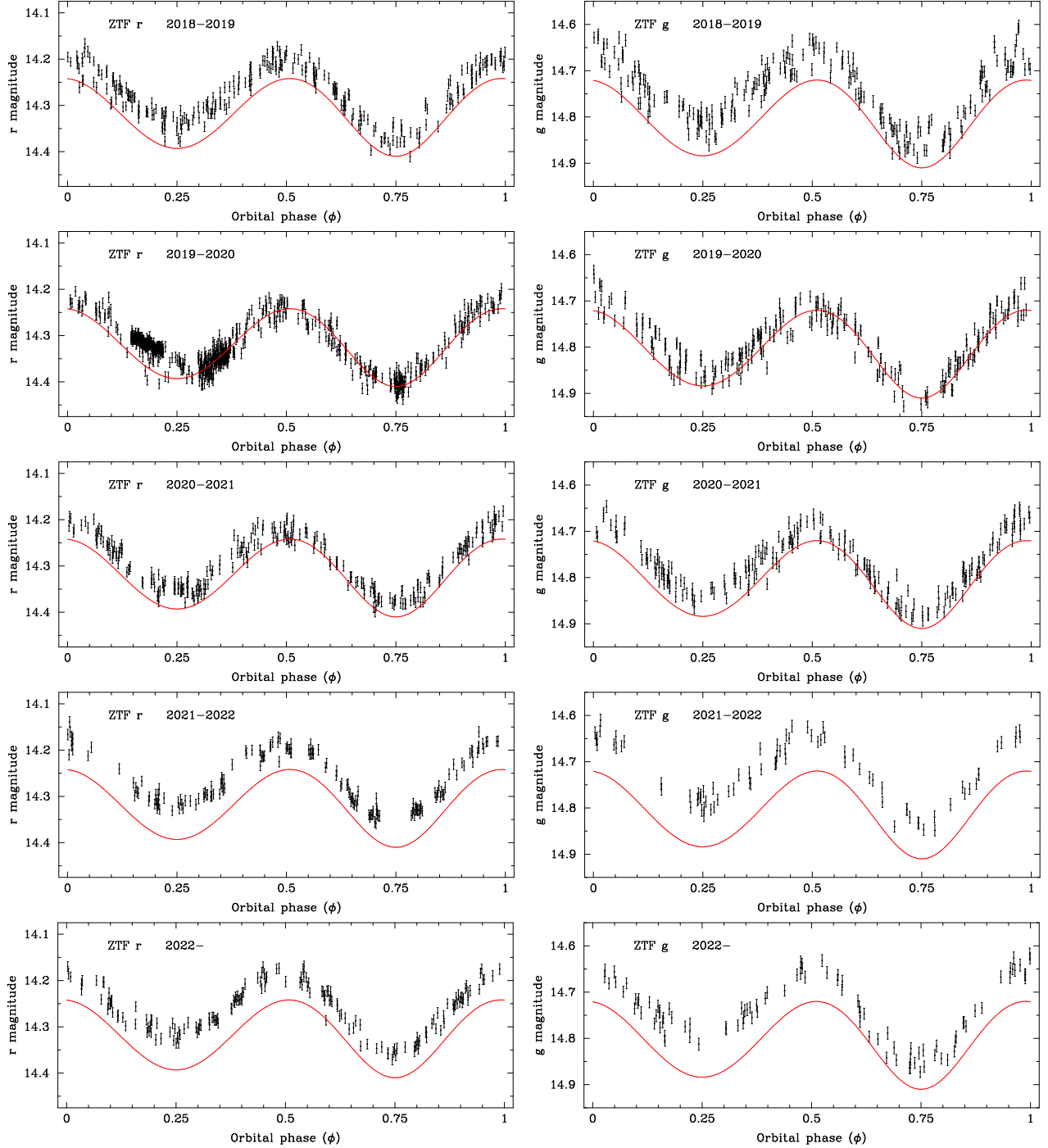


**Figure 4.** ZTF observations of 3FGL J0212.1+5320 in  $r$  and  $g$ , folded according to the orbital ephemeris calculated from the MDM data (see Section 5.2). Each panel contains data from one annual observing season. The red curve is the same pure ellipsoidal model used in Figure 3, here normalized to the faintest state, which is represented by the 2019–2020 observing season. Linear limb-darkening coefficients of 0.5 and 0.7 were used for  $r$  and  $g$ , respectively.

and FPMB) combined, in the 3–79 keV band as a function of binary orbital phase binned in 5000 s intervals is shown in Figure 5. The count rate in each bin has been corrected for the fractional exposure caused by gaps in the data due to occultation by the Earth as the telescope moves in its orbit. Large-amplitude variability, with a factor of  $\sim 2$  range in flux, is clearly seen from 3FGL J0212.1+5320 and appears to repeat in the two full orbital cycles covered. The variability pattern, with a trough and peak at phases  $\phi \approx 0.25$  and  $\phi \approx 0.75$ , respectively, appears to follow the typical X-ray behavior of redbacks (see, e.g, Bogdanov et al. 2011, 2014a,b; Gentile et al. 2014; Al Noori et al. 2018; Bogdanov et al. 2021), which is interpreted as being due to the changing view of the intrabinary shock. This intrabinary shock forms at the interface between the relativistic pulsar wind and the outflow from the secondary star (Arons & Tavani 1993). For reference, we also show a light curve based on the archival 30 ks Chandra ACIS-S 0.3–8 keV exposure of the field around 3FGL J0212.1+5320 (ObsId 14814<sup>2</sup>) obtained on 2013 August 22 (originally presented in Li et al. 2016 and Linares et al. 2017). The Chandra light curve covers  $\approx 40\%$  of the binary orbit around the X-ray maximum at  $\phi \approx 0.75$ , with count rates as a function of orbital phase generally consistent with those seen in the NuSTAR data.

The NuSTAR FPMA and FPMB time-averaged spectra (Figure 6) are well fit ( $\chi^2 = 109.47$  for 136 degrees of freedom) by an absorbed power law assuming the `tbabs` model of interstellar absorption and chemical abundances from Wilms et al. (2000). There is no evidence for a spectral turnover at higher energies in the best fit residuals. The best fit parameter values we obtain are  $N_{\text{H}} < 1.7 \times 10^{22} \text{ cm}^{-2}$  for the hydrogen column density along the line of sight,  $\Gamma = 1.35_{-0.06}^{+0.08}$  for the spectral photon index, and a  $F_X = (5.3 \pm 0.4) \times 10^{-12} \text{ erg cm}^{-2} \text{ s}^{-1}$  (3–79 keV) for the unabsorbed flux, with the upper limit and all uncertainties quoted at the 90% confidence level for one interesting parameter. For  $N_{\text{H}}$  fixed at the best fit value of  $1.4 \times 10^{21} \text{ cm}^{-2}$  from the fit to the Chandra data<sup>3</sup> reported by Linares et al. (2017), we obtain comparable results with  $\Gamma = 1.35 \pm 0.06$  and  $F_X = (5.3 \pm 0.4) \times 10^{-12} \text{ erg cm}^{-2} \text{ s}^{-1}$ . For a distance of 1.16 kpc, this corresponds to a 3–79 keV luminosity of  $L_X = 8.6 \times 10^{32} \text{ erg s}^{-1}$ .

## 6.2. *Swift* XRT

The Neil Gehrels Swift Observatory has targeted 3FGL J0212.1+5320 in 15 snapshot observations. We used HEASoft version 6.28 to process all XRT observations taken in photon counting mode, and produced

<sup>2</sup> Available at <https://doi.org/10.25574/14814>.

<sup>3</sup> As the archival Chandra ACIS observation only has partial orbital coverage ( $\approx 40\%$ ) joint spectroscopy with NuSTAR is not feasible.

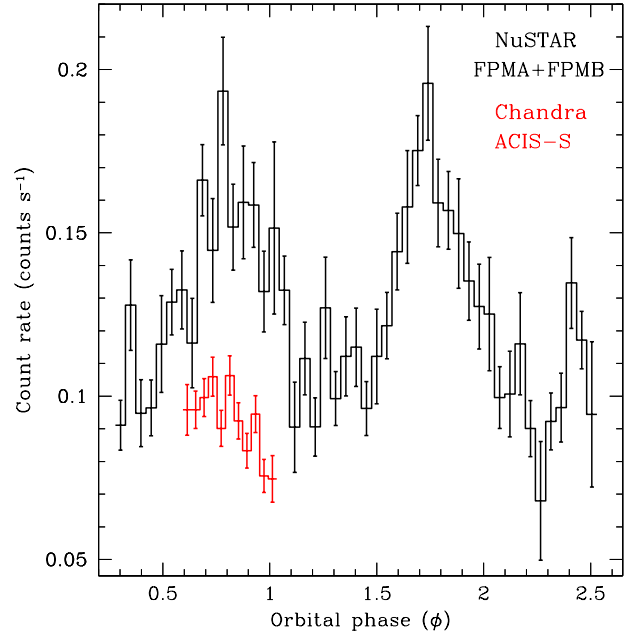


**Figure 5.** NuSTAR FPMA+FPMB 3–79 keV background-subtracted light curve of 3FGL J0212.1+5320 binned at a resolution of 3600 s (black) and Chandra ACIS-S 0.3–8 keV light curve binned at 3000 s (red). The NuSTAR count rates have been corrected for fractional exposures in each bin caused by Earth occultation.

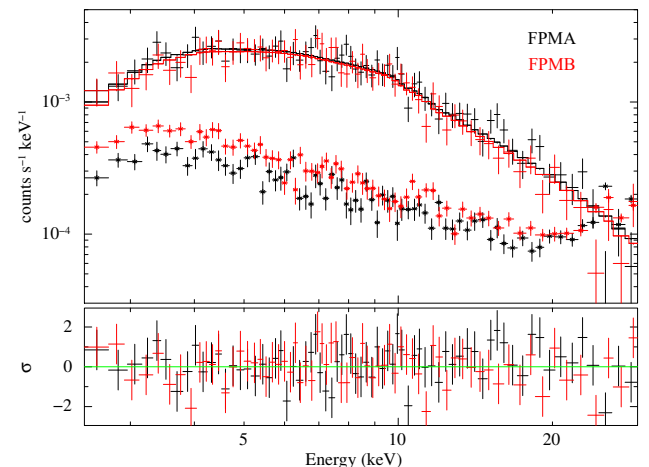


**Figure 6.** Time-averaged NuSTAR FPMA (black) and FPMB (red) spectra of 3FGL J0212.1+5320 fit with an absorbed power-law model. The stars show the background spectra for each detector. The bottom panel shows the best fit residuals expressed in terms of standard deviation with error bars of size  $1\sigma$ . See Section 6.1 for best fit parameters.

background-subtracted light curves in the 0.3–10 keV band using the clean Level 2 event files. We used an aperture radius of 25 pixels ( $59''$ ) for the source and 50 pixels ( $118''$ ) for the background region. Within the

good time intervals (GTIs), we found the correction factors for bad columns in each 10 s time interval, and applied them to 60 s time bins of the light curve. Using the 60 s bins, we subtracted the background rate from the corrected source rate. The mean net count rate per observation is outlined in Table 4 and shown in Figure 8.

To obtain sufficient statistics for spectral fitting, we group all 15 observations. We combined the exposure maps using `ximage`, and the clean Level 2 files, and extracted a spectrum from the final image using the extraction regions used in our light curves. We generated the ancillary response file using the tool `xrtmkarf`, which corrects for hot columns and bad pixels, and applied the point-spread-function correction. We used `grppha` to bin the counts in energy, ignoring energies  $< 0.3$  keV. We used `group min 20` to ensure that there are at least 20 counts per bin in order to employ  $\chi^2$  statistics.

Using XSPEC, we fit an absorbed power-law model and integrated the flux over a 0.3–10 keV range. Using the same  $N_{\text{H}}$  of  $1.4 \times 10^{21} \text{ cm}^{-2}$  (Linares et al. 2017) as in Section 6.1, we obtain  $\Gamma = 1.18 \pm 0.16$  and  $F_X = (1.07 \pm 0.15) \times 10^{-12} \text{ erg cm}^{-2} \text{ s}^{-1}$ , which corresponds to a luminosity of  $L_X = 1.72 \times 10^{32} \text{ erg s}^{-1}$ . Extrapolating this to the broader high-energy coverage of NuSTAR, we find the fluxes are consistent with each other.

### 6.3. *Swift UVOT*

Along with the XRT, 3FGL J0212.1+5320 was also observed with the UV/Optical Telescope (UVOT) with four of its six filters (*U*, *UVW1*, *UVM2*, and *UVW2*). The photometry was extracted using the `uvotsource` command in FTOOLS. The net flux was obtained from an aperture of  $5''$  radius for the source and  $20''$  for the background region. Magnitudes are in the AB system (Breeveld et al. 2011). Table 5 shows a log of the observations, including the magnitude for each image in a single filter for each observation.

In order to interpret the Swift UVOT measurements relative to the ground-based optical, we have to take into account the expected magnitudes of the F6 type companion star (Linares et al. 2017) as well as the significant extinction at this low Galactic latitude of  $7^\circ$ . The most precise measurements are in the *U* filter; we examined these as a function of orbital phase, finding that their variation by  $\approx 0.28$  mag is in accord with the phasing of ellipsoidal modulation (see Figure 7), although with additional scatter arising from long-term variability as is observed at visible wavelengths.

For quantitative comparison with our *V*-band measurements in Figure 3, we convert from the AB system to the Vega system using  $U_{\text{AB}} - U_{\text{Vega}} = +1.02$ . Green et al. (2019) evaluate the extinction as  $E(g-r) = 0.12 \pm 0.02$  mag at  $d = 1.15$  kpc, which corresponds to  $A_V = 0.41$  mag and  $E(U-V) = 0.24$  mag. With these conversions and corrections applied, the intrinsic color  $U_0 - V_0 = (U - V) - E(U - B)$  ranges from 0.41–0.49,

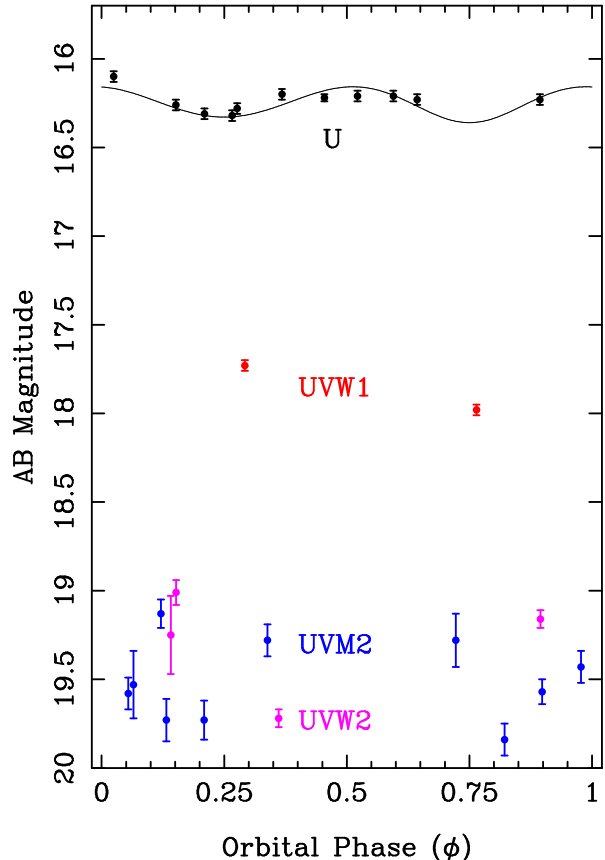


**Figure 7.** Swift UVOT magnitudes from Table 5, plotted as a function of orbital phase using the optical ephemeris of Table 3. The ellipsoidal model is superposed on the *U* points.

which is consistent with the expected  $U_0 - V_0 \approx 0.47$  for an F6 main sequence star. Therefore, the *U*-band magnitude and its variation are consistent with photospheric emission.

The *UVW1*, *UVM2*, and *UVW2* measurements are more difficult to interpret either because they are sparse, their error bars are larger, and especially because extinction corrections are highly uncertain in these broad-band filters when the extinction is large (see Table 4 of Siegel et al. 2014). The UV filter points are more variable than the *U*-band, but in Figure 7 they have no clear trend with orbital phase, e.g., like the X-ray light curve.

## 7. DISCUSSION

### 7.1. *Orbital Parameters*

In the absence of more extensive orbital coverage of the pulsar, the binary parameters modelled by Shahbaz et al. (2017) can be used to check for compatibility with the pulsar timing results of Table 2 by predicting the apparent spin period derivative  $\dot{P}_s$  at any orbital phase due to the acceleration. For a circular orbit in the non-

relativistic limit,

$$P_s = P_{s,0} \left[ 1 + \frac{K_2 q}{c} \cos(2\pi\phi) \right], \quad (2)$$

$$\dot{P}_s = -\frac{2\pi K_2 q}{c} \frac{P_{s,0}}{P_b} \sin(2\pi\phi), \quad (3)$$

where  $P_{s,0}$  is the intrinsic spin period,  $K_2 = 216.5_{-5.7}^{+5.8}$  km s<sup>-1</sup> is the radial velocity amplitude of the companion, and  $q = 0.28_{-0.09}^{+0.08}$  is the mass ratio. We choose to apply these to Obs 05 with its longer detection, using  $\phi = 0.698$ , its optically determined starting phase (Table 1). The prediction is then  $\dot{P}_s = (3.39 \pm 1.09) \times 10^{-11}$  s s<sup>-1</sup>. Its accuracy is limited mainly by the  $\approx 30\%$  uncertainty in the mass ratio  $q$ , as well as by additional model-dependent uncertainty in  $q$  when choosing authors' favored hot-spot model and neglecting their (dark) starspot model. The PRESTO measured  $\dot{P}_s$  of Obs 05 is  $(2.987 \pm 0.011) \times 10^{-11}$  s s<sup>-1</sup> (Table 2), which is consistent with the predicted value within its uncertainty, thus supporting the identification of the pulsar with the optical binary.

Since  $\dot{P}_s$  is measured more precisely than  $q$  is modelled from the optical, we now invert Equation (3) and solve for  $q$  more accurately and precisely. Since  $K_2$  is virtually model-independent (to within  $\approx 1$  km s<sup>-1</sup>, Shahbaz et al. 2017), the resulting model-independent value of  $q$  is  $0.2469 \pm 0.0067$ . In addition we posit a systematic uncertainty of 0.03 on the optically determined orbital phase  $\phi$  (see below), which would correspond to an error of 0.010 on  $q$ . The model-independent  $P_{s,0}$  is 2.1147012(46) ms, but 2.1147(1) ms with error dominated by orbital phase uncertainty. Finally, the projected semi-major axis of the pulsar's orbit is

$$\frac{a_1 \sin i}{c} = \frac{P_b K_2 q}{2\pi c} = \frac{-\dot{P}_s P_b^2}{4\pi^2 P_{s,0} \sin(2\pi\phi)} = 2.132 \pm 0.008 \text{ lt-s}. \quad (4)$$

A 0.03 uncertainty on  $\phi$  would also add a dominant systematic error of 0.09 lt-s on  $a_1 \sin i/c$ . Together with the well-measured  $P_{s,0}$  and  $P_b$ , the bound on  $a_1 \sin i$  will be valuable in searching for  $\gamma$ -ray pulsations.

These orbital parameters imply a minimum companion mass of  $M_2 > 0.35 M_\odot$  for an assumed typical  $M_1 = 1.4 M_\odot$  primary. If the inclination angle  $i = 69^\circ$  from the hot-spot model of Shahbaz et al. (2017) is correct, then the masses become  $M_1 = 1.75 M_\odot$  and  $M_2 = 0.43 M_\odot$ . If  $i = 64.95^\circ$  as in their dark-spot model, then  $M_1 = 1.93 M_\odot$  and  $M_2 = 0.48 M_\odot$ .

Finally, we fit the apparent spin parameters measured from both radio detections using PRESTO's `fitorb`, which uses the Blandford & Teukolsky (1976) binary model, to calculate preliminary parameters of the pulsar's orbit. While pulsar timing should be used to further refine these parameters, we do not yet have enough observations to obtain such a solution. Here, our goal is

to simply test for consistency with the optically-derived ephemeris.

We allowed for eccentricity in the fit and found  $e = 0$ , consistent with the near-perfect circular orbits of redbacks. We find an intrinsic spin period  $P_{s,0} = 2.11461962(94)$ , an orbital period  $P_b = 0.869573849(10)$  days, a projected semi-major axis  $(a_1/c) \sin i = 2.02169 \pm 0.00015$  lt-s, and an epoch of ascending node  $T_{\text{asc}} = 59757.87757(36)$  BMJD (after using the optical ephemeris extrapolated to midpoint of the two radio detections to make an initial guess of  $T_{\text{asc}} = 59757.90718$ ). While  $P_b$  is within  $2\sigma$  of the optical photometric value and error listed in Table 3,  $T_{\text{asc}}$  comes 0.034 cycles later than the prediction from the optical  $T_0$ , a difference that we verified by folding the optical data on the radio parameters. This phase discrepancy can also account for the 0.11 lt-s difference in the projected semi-major axis compared with that derived above using an optically predicted phase, as well as the 0.00008 ms difference in the intrinsic spin period.

Recall that systematic error likely dominates the uncertainty of the optical  $T_0$  because it is not a kinematic parameter, but a photometric property in the context of an idealized ellipsoidal model. With regard to the radio, the two widely spaced detections obtained so far do not permit a phase-connected timing solution, nor provide many pulse times of arrival (TOAs) with which to carry out a long-term timing analysis and obtain precise parameters. As a result, the intrinsic spin-down rate and spin-down power of the pulsar are not yet measured. We expect that denser radio timing will pin down all of these parameters, including the time of ascending node.

## 7.2. Eclipses and Flux Variability

Despite observing at inferior conjunction of the pulsar, the non-detections (Obs 01, 02, and 04) and variations in pulsar signal intensity across both time and frequency during the two detections is not unusual in redbacks as seen in PSR J1048+2339 (Deneva et al. 2016). This suggests a possible gas cloud or an extended companion wind surrounding the pulsar (Crawford et al. 2013), which could be related to the long-term optical flux variability we see (Section 5.1). Eclipses covering a large fraction of the orbit are typical for redbacks ( $\sim 50\%$ ), especially for tMSPs (Archibald et al. 2009; Roy et al. 2014). This is due to redbacks having short orbital periods and large companions, as opposed to black widows which have been observed to have shorter eclipses ( $\sim 0.1 - 0.2 P_b$ : Polzin et al. 2018, 2020; Crowter et al. 2020; Deneva et al. 2021; Ray et al. 2022).

Both of our detections (Obs 03 and Obs 05) occur just before inferior conjunction of the pulsar ( $\phi = 0.75$ ). Although we do not assume that the detections are dependent only on orbital phase, a Smoothed Particle Hydrodynamics (SPH) simulation of the redback PSR B1744-24A showed the strong companion wind flowing behind and lagging the pulsar due to the combined

effects of gravity, gas pressure, and the Coriolis force (Tavani & Brookshaw 1991, 1993). This kind of asymmetric wind geometry would cause  $\phi = 0.75$ – $0.25$  to be eclipsed, while  $\phi = 0.25$ – $0.75$  would be visible, which is what we have observed so far (Table 1). However, the Brookshaw & Tavani (1995) simulations show pulsar enshrouding can occur for orbital periods  $\lesssim 10$  hr – a threshold that some redbacks, including this one, exceed.

In addition to absorption due to intrabinary material, another mechanism for the nondetections could be due to the interstellar medium (ISM) along the line of sight contributing to its dimming/brightening (Lorimer & Kramer 2004) since interstellar scintillation is stronger at lower DMs and has no preferred orbital phase (Cordes et al. 1985; Camilo et al. 2000; D’Amico et al. 2001a). PSR J1048+2339, for example, revealed the effects of scintillation after incurring different flux densities between observations at three different observing frequencies (Deneva et al. 2016). The bright signal confined to the top of our frequency band near  $\sim 1.8$  GHz in Obs 05 (Figure 2) and the narrow-band scintles suggests that it could be caused by scintillation since it does not occur in Obs 03, it covers a very narrow range of frequencies, and the pulsar is much dimmer in the rest of the band.

Unlike the DM delays observed preceding black widow eclipses (PSR J1544+4937 Bhattacharyya et al. 2013 and PSR J1810+1744 Polzin et al. 2018), PSR J1227–4853 (Kudale et al. 2020) and PSR 1744–24A (Nice & Thorsett 1992) have been shown to exhibit occasional delays outside of its eclipse-associated phases. Nice & Thorsett (1992) observed PSR B1744–24A in Terzan 5 at several frequencies, and noted long-term disappearances at all frequencies, with evidence that they could be episodic in nature rather than random. PSR J1740–5340 in the globular cluster NGC 6397 exhibits eclipses around superior conjunction of the pulsar for 40% of its orbit, as well as random DM variations over a wide range of orbital phases (D’Amico et al. 2001b), while the newly found PSR J1740–5340b exhibits eclipses for 50% of its orbit (Zhang et al. 2022). PSR J2039–5617 (Corongiu et al. 2021), PSR J1048+2339 (Deneva et al. 2016), and J1417–4402 (Camilo et al. 2016) also undergo eclipses for roughly half their orbit. PSR J1723–2837 was also found to exhibit flux variability and have non-detections at phases away from superior conjunction of the pulsar (Crawford et al. 2013). Kudale et al. (2020) conducted pulsed and continuum flux densities of PSR J1227–4853 and suggested cyclotron absorption by the magnetic field of the companion as a potential cause for eclipses and occasional fading, building on the original mechanism suggestion by Thompson et al. (1994) for the BW PSR B1957+20. Based on our observations and the fading behavior seen in Figure 1, we suspect PSR J0212+5321 to also be similarly eclipsed.

The timing anomaly observed in Obs 05 and described in Section 4.4 is not uncommon in eclipsing MSPs. Such kinks in timing have also been observed in 3FGL J1417.5–4402 (PSR J1417–4402; Camilo et al. 2016). They could be caused by mass transfer through the L2 point during a previously unobserved accretion-powered state (Kudale et al. 2020). Removing the kink does not affect our observed parameters, and, as a result, does not affect our derived orbital parameters. This is because the pulses during the kink do not contribute significantly to the peak of the summed pulse profile.

## 8. CONCLUSIONS

We have discovered the suspected rotation-powered MSP in the 3FGL J0212.1+5320 gamma-ray system with the Robert C. Byrd Green Bank Telescope using the L-band receiver at a center frequency of 1501 MHz utilizing the Breakthrough Listen digital receiver. PSR J0212+5321 is a  $P = 2.11$  ms radio pulsar with a DM of  $25.7 \text{ pc cm}^{-3}$ . PSR J0212+5321 joins three other recently discovered redbacks: PSR J0838–2827, J0955–3949 and J2333–5526, found by the TRAPUM collaboration<sup>4</sup>(Clark et al. 2023). PSR J0212+5321’s detection makes it one of the longest binary period eclipsing MSPs known.

The acceleration of PSR J0212+5321 inferred from the apparent change of the spin period over time is consistent with being due to its motion in the 20.9 hour orbit determined from optical observations. The distance to the pulsar estimated from the DM is in good agreement with the Gaia parallax-derived distance. Its pulsed radio emission appears to be intermittent on timescales of weeks/months possibly due to interstellar scintillation and variable outflows of plasma from the companion star that occasionally enshrouds the pulsar.

The NuSTAR observations presented here provide the first complete coverage of the binary orbit in X-rays, which reveals a hard non-thermal spectrum and a flux variability pattern commonly seen in redbacks. Such X-ray characteristics can be attributed to an intra-binary shock formed at the interface of the winds from the two stars. These data can provide important input for validating and improving recently developed semi-analytic models of the wind interaction in redbacks and black widows (Romani & Sanchez 2016; Wadiasingh et al. 2017; Kandel et al. 2019; van der Merwe et al. 2020; Cortés & Sironi 2022). The implied X-ray luminosity is one of the highest recorded among redbacks in the pulsar state and black widow MSPs in the Galactic field (Linares 2014; Linares et al. 2017), followed by tMSPs PSR J1023+0038 and XSS J12270–4859 (Archibald et al. 2009; Bogdanov et al. 2011; Roy et al. 2014; Bogdanov et al. 2014b, 2021). The Swift XRT and UVOT coverage is fairly sparse and shows no evidence of large-

<sup>4</sup> Discoveries listed at <http://www.trapum.org/discoveries/>.

amplitude X-ray variability. Judging from the lack of any significant flux changes in the long term Fermi LAT  $\gamma$ -ray light curve (see Figure 8 in the Appendix), there is no indication that the pulsar was accreting at the time of the radio non-detections nor at any prolonged interval in the past 14 years. However, the X-ray-to- $\gamma$ -ray flux ratio of 10% shows that it is consistent with known tMSPs, which are significantly larger than those of most redbacks ( $\leq 1\%$ ; Li et al. 2016). This makes PSR J0212+5321 a strong tMSP candidate that may transition to a disk state in the near future and thus warrants continued close monitoring at all wavelengths.

Future observations and long-term timing of PSR J0212+5321 will allow us to measure its spin period derivative to calculate its spin-down luminosity,  $\dot{E}$ , which is likely one of the highest among MSPs based on its high X-ray luminosity. Although flaring behavior has not been observed in the companion like in other redbacks, the spin-down power of the pulsar is also an important factor in the energy budget of flares and any persistent heating of the companion’s photosphere (Halpern et al. 2022). A timing solution will also allow for the detection of  $\gamma$ -ray pulsations, and X-ray/UV pulsations in the event that it switches to a radio-quiet disk-dominated state; thus, serving as an additional laboratory for studying the poorly understood transition mechanism of MSPs.

Conducting longer observations with a wider orbital phase coverage beyond inferior conjunction of the pulsar will help us understand the non-detections and determine the fraction of the pulsar that is eclipsed. It will also help identify any strong contrast in excess DM between these occasional delays and those occurring at the eclipse boundaries, while probing the potential effect of the magnetic field. Due to the observed pulsar brightness towards higher frequencies at L-band presented here, observations at higher frequencies, like S-band, will also help determine any frequency dependence of eclipse durations (Polzin et al. 2020), a possible low-frequency cutoff due to absorption, and a spectral index.

While any new available data with MDM, ZTF, Swift, NuSTAR, and Fermi will continue to be monitored and analyzed, now that the pulsar in the 3FGL J0212.1+5320 system has been detected, obtaining a radio-derived timing solution is the next step to understanding this system and will provide valuable information beyond that which optical and X-ray telescopes have so far revealed. However, given the intermittency of radio detections, it might be more feasible to obtain a  $\gamma$ -ray timing solution.

#### ACKNOWLEDGMENTS

We thank the anonymous referee for a careful reading, several clarifications, and requests for useful additional information.

Breakthrough Listen is managed by the Breakthrough Initiatives, sponsored by the Breakthrough Prize Foundation. The Green Bank Observatory is a facility of the National Science Foundation, operated under cooperative agreement by Associated Universities, Inc. We thank the staff at Breakthrough Listen and the Green Bank Observatory for their operational support.

We acknowledge use of computing resources from Columbia University’s Shared Research Computing Facility project, which is supported by NIH Research Facility Improvement Grant 1G20RR030893-01, and associated funds from the New York State Empire State Development, Division of Science Technology and Innovation (NYSTAR) Contract C090171, both awarded April 15, 2010.

Support for this work was provided in part by NASA NuSTAR General Observer Program grant 80NSSC21K0019 and NASA Swift Guest Investigator Program grant 80NSSC21K1380.

The MDM Observatory is operated by Dartmouth College, Columbia University, The Ohio State University, Ohio University, and the University of Michigan. We thank Manuel Linares for sharing optical photometry data.

This work made use of observations obtained with the Samuel Oschin Telescope 48-inch and the 60-inch Telescope at the Palomar Observatory as part of the Zwicky Transient Facility project. ZTF is supported by the National Science Foundation under Grants No. AST-1440341 and AST-2034437 and a collaboration including current partners Caltech, IPAC, the Weizmann Institute for Science, the Oskar Klein Center at Stockholm University, the University of Maryland, Deutsches Elektronen-Synchrotron and Humboldt University, the TANGO Consortium of Taiwan, the University of Wisconsin at Milwaukee, Trinity College Dublin, Lawrence Livermore National Laboratories, IN2P3, University of Warwick, Ruhr University Bochum, Northwestern University and former partners the University of Washington, Los Alamos National Laboratories, and Lawrence Berkeley National Laboratories. Operations are conducted by COO, IPAC, and UW.

This work is based in part on data from the European Space Agency (ESA) mission *Gaia* (<https://www.cosmos.esa.int/gaia>), processed by the *Gaia* Data Processing and Analysis Consortium (DPAC, <https://www.cosmos.esa.int/web/gaia/dpac/consortium>). Funding for the DPAC has been provided by national institutions, in particular the institutions participating in the *Gaia* Multilateral Agreement.

This research has made use of data and software provided by the High Energy Astrophysics Science Archive Research Center (HEASARC), which is a service of the Astrophysics Science Division at NASA/GSFC, the NuSTAR Data Analysis Software (NuSTARDAS) jointly developed by the ASI Space Science Data Center (SSDC, Italy) and the California Institute of Tech-

nology (Caltech, USA), data from the Chandra Data Archive, and software provided by the Chandra X-ray Center (CXC) in the application packages CIAO.

This work has relied on NASA's Astrophysics Data System (ADS) Bibliographic Services and the ArXiv.

*Facilities:* GBT, McGraw-Hill, NuSTAR, Swift

*Software:* PRESTO (Ransom 2001), DSPSR (van Straten & Bailes 2011), HEASoft (NASA High Energy Astrophysics Science Archive Research Center (Heasarc) 2014)

## REFERENCES

- Abdo, A. A., Ackermann, M., Ajello, M., et al. 2010, *ApJS*, 188, 405, doi: [10.1088/0067-0049/188/2/405](https://doi.org/10.1088/0067-0049/188/2/405)
- Abdo, A. A., Ajello, M., Allafort, A., et al. 2013, *ApJS*, 208, 17, doi: [10.1088/0067-0049/208/2/17](https://doi.org/10.1088/0067-0049/208/2/17)
- Al Noori, H., Roberts, M. S. E., Torres, R. A., et al. 2018, *ApJ*, 861, 89, doi: [10.3847/1538-4357/aac828](https://doi.org/10.3847/1538-4357/aac828)
- Alpar, M. A., Cheng, A. F., Ruderman, M. A., & Shaham, J. 1982, *Nature*, 300, 728, doi: [10.1038/300728a0](https://doi.org/10.1038/300728a0)
- Andersen, B. C., & Ransom, S. M. 2018, *ApJL*, 863, L13, doi: [10.3847/2041-8213/aad59f](https://doi.org/10.3847/2041-8213/aad59f)
- Archibald, A. M., Stairs, I. H., Ransom, S. M., et al. 2009, *Science*, 324, 1411, doi: [10.1126/science.1172740](https://doi.org/10.1126/science.1172740)
- Arons, J., & Tavani, M. 1993, *ApJ*, 403, 249, doi: [10.1086/172198](https://doi.org/10.1086/172198)
- Backer, D., Kulkarni, S. R., Heiles, C., M, M. D., & W, M. G. 1982, *Nature*, 300, 615, doi: [10.1038/300615a0](https://doi.org/10.1038/300615a0)
- Barr, E. D., Champion, D. J., Kramer, M., et al. 2013, *Monthly Notices of the Royal Astronomical Society*, 435, 2234, doi: [10.1093/mnras/stt1440](https://doi.org/10.1093/mnras/stt1440)
- Bassa, C. G., Patruno, A., Hessels, J. W. T., et al. 2014, *MNRAS*, 441, 1825, doi: [10.1093/mnras/stu708](https://doi.org/10.1093/mnras/stu708)
- Bellm, E. C., Kaplan, D. L., Breton, R. P., et al. 2016, *The Astrophysical Journal*, 816, 74, doi: [10.3847/0004-637x/816/2/74](https://doi.org/10.3847/0004-637x/816/2/74)
- Bellm, E. C., Kaplan, D. L., Breton, R. P., et al. 2016, *ApJ*, 816, 74, doi: [10.3847/0004-637X/816/2/74](https://doi.org/10.3847/0004-637X/816/2/74)
- Bellm, E. C., Kulkarni, S. R., Graham, M. J., et al. 2019, *PASP*, 131, 018002, doi: [10.1088/1538-3873/aaecbe](https://doi.org/10.1088/1538-3873/aaecbe)
- Bhattacharya, D., & van den Heuvel, E. 1991, *Physics Reports*, 203, 1, doi: [https://doi.org/10.1016/0370-1573\(91\)90064-S](https://doi.org/10.1016/0370-1573(91)90064-S)
- Bhattacharyya, B., Roy, J., Ray, P. S., et al. 2013, *The Astrophysical Journal Letters*, 773, L12, doi: [10.1088/2041-8205/773/1/L12](https://doi.org/10.1088/2041-8205/773/1/L12)
- Blandford, R., & Teukolsky, S. A. 1976, *ApJ*, 205, 580, doi: [10.1086/154315](https://doi.org/10.1086/154315)
- Bogdanov, S., Archibald, A. M., Hessels, J. W. T., et al. 2011, *ApJ*, 742, 97, doi: [10.1088/0004-637X/742/2/97](https://doi.org/10.1088/0004-637X/742/2/97)
- Bogdanov, S., Bahramian, A., Heinke, C. O., et al. 2021, *ApJ*, 912, 124, doi: [10.3847/1538-4357/abee78](https://doi.org/10.3847/1538-4357/abee78)
- Bogdanov, S., Esposito, P., Crawford, Fronefield, I., et al. 2014a, *ApJ*, 781, 6, doi: [10.1088/0004-637X/781/1/6](https://doi.org/10.1088/0004-637X/781/1/6)
- Bogdanov, S., Patruno, A., Archibald, A. M., et al. 2014b, *ApJ*, 789, 40, doi: [10.1088/0004-637X/789/1/40](https://doi.org/10.1088/0004-637X/789/1/40)
- Breeveld, A. A., Landsman, W., Holland, S. T., et al. 2011, in *American Institute of Physics Conference Series*, Vol. 1358, *Gamma Ray Bursts 2010*, ed. J. E. McEnery, J. L. Racusin, & N. Gehrels, 373–376, doi: [10.1063/1.3621807](https://doi.org/10.1063/1.3621807)
- Brookshaw, L., & Tavani, M. 1995, in *Astronomical Society of the Pacific Conference Series*, Vol. 72, *Millisecond Pulsars. A Decade of Surprise*, ed. A. S. Fruchter, M. Tavani, & D. C. Backer, 244
- Camilo, F., Lorimer, D. R., Freire, P., Lyne, A. G., & Manchester, R. N. 2000, *ApJ*, 535, 975, doi: [10.1086/308859](https://doi.org/10.1086/308859)
- Camilo, F., Reynolds, J. E., Ransom, S. M., et al. 2016, *The Astrophysical Journal*, 820, 6, doi: [10.3847/0004-637X/820/1/6](https://doi.org/10.3847/0004-637X/820/1/6)
- Cho, P. B., Halpern, J. P., & Bogdanov, S. 2018, *ApJ*, 866, 71, doi: [10.3847/1538-4357/aade92](https://doi.org/10.3847/1538-4357/aade92)
- Claret, A., & Bloemen, S. 2011, *A&A*, 529, A75, doi: [10.1051/0004-6361/201116451](https://doi.org/10.1051/0004-6361/201116451)
- Clark, C. J., Nieder, L., Voisin, G., et al. 2020, *Monthly Notices of the Royal Astronomical Society*, 502, 915, doi: [10.1093/mnras/staa3484](https://doi.org/10.1093/mnras/staa3484)
- Clark, C. J., Breton, R. P., Barr, E. D., et al. 2023, *Monthly Notices of the Royal Astronomical Society*, 519, 5590, doi: [10.1093/mnras/stac3742](https://doi.org/10.1093/mnras/stac3742)
- Cordes, J. M., & Lazio, T. J. W. 2002, arXiv e-prints, astro. <https://arxiv.org/abs/astro-ph/0207156>
- . 2003, arXiv e-prints, astro. <https://arxiv.org/abs/astro-ph/0301598>
- Cordes, J. M., Weisberg, J. M., & Boriakoff, V. 1985, *ApJ*, 288, 221, doi: [10.1086/162784](https://doi.org/10.1086/162784)
- Corongiu, A., Mignani, R. P., Seyffert, A. S., et al. 2021, *MNRAS*, 502, 935, doi: [10.1093/mnras/staa3463](https://doi.org/10.1093/mnras/staa3463)
- Cortés, J., & Sironi, L. 2022, *ApJ*, 933, 140, doi: [10.3847/1538-4357/ac74b2](https://doi.org/10.3847/1538-4357/ac74b2)
- Crawford, F., Lyne, A. G., Stairs, I. H., et al. 2013, *ApJ*, 776, 20, doi: [10.1088/0004-637X/776/1/20](https://doi.org/10.1088/0004-637X/776/1/20)
- Crowter, K., Stairs, I. H., McPhee, C. A., et al. 2020, *MNRAS*, 495, 3052, doi: [10.1093/mnras/staa933](https://doi.org/10.1093/mnras/staa933)

- D'Amico, N., Lyne, A. G., Manchester, R. N., Possenti, A., & Camilo, F. 2001a, *ApJL*, 548, L171, doi: [10.1086/319096](https://doi.org/10.1086/319096)
- D'Amico, N., Possenti, A., Manchester, R. N., et al. 2001b, *ApJL*, 561, L89, doi: [10.1086/324562](https://doi.org/10.1086/324562)
- Deneva, J. S., Ray, P. S., Camilo, F., et al. 2016, *The Astrophysical Journal*, 823, 105, doi: [10.3847/0004-637x/823/2/105](https://doi.org/10.3847/0004-637x/823/2/105)
- Deneva, J. S., Ray, P. S., Camilo, F., et al. 2021, *ApJ*, 909, 6, doi: [10.3847/1538-4357/abd7a1](https://doi.org/10.3847/1538-4357/abd7a1)
- Edmonds, P. D., Gilliland, R. L., Camilo, F., Heinke, C. O., & Grindlay, J. E. 2002, *The Astrophysical Journal*, 579, 741, doi: [10.1086/342985](https://doi.org/10.1086/342985)
- Frail, D. A., Jagannathan, P., Mooley, K. P., & Intema, H. T. 2016, *The Astrophysical Journal*, 829, 119, doi: [10.3847/0004-637X/829/2/119](https://doi.org/10.3847/0004-637X/829/2/119)
- Fruchter, A. S., Stinebring, D. R., & Taylor, J. H. 1988, *Nature*, 333, 237, doi: [10.1038/333237a0](https://doi.org/10.1038/333237a0)
- Gaia Collaboration, Prusti, T., de Bruijne, J. H. J., et al. 2016, *A&A*, 595, A1, doi: [10.1051/0004-6361/201629272](https://doi.org/10.1051/0004-6361/201629272)
- Gaia Collaboration, Vallenari, A., Brown, A. G. A., et al. 2022, arXiv e-prints, arXiv:2208.00211. <https://arxiv.org/abs/2208.00211>
- Gentile, P. A., Roberts, M. S. E., McLaughlin, M. A., et al. 2014, *ApJ*, 783, 69, doi: [10.1088/0004-637X/783/2/69](https://doi.org/10.1088/0004-637X/783/2/69)
- Gomel, R., Faigler, S., & Mazeh, T. 2021, *MNRAS*, 501, 2822, doi: [10.1093/mnras/staa3305](https://doi.org/10.1093/mnras/staa3305)
- Green, G. M., Schlafly, E., Zucker, C., Speagle, J. S., & Finkbeiner, D. 2019, *ApJ*, 887, 93, doi: [10.3847/1538-4357/ab5362](https://doi.org/10.3847/1538-4357/ab5362)
- Halpern, J. P., Perez, K. I., & Bogdanov, S. 2022, *ApJ*, 935, 151, doi: [10.3847/1538-4357/ac8161](https://doi.org/10.3847/1538-4357/ac8161)
- Harrison, F. A., Craig, W. W., Christensen, F. E., et al. 2013, *ApJ*, 770, 103, doi: [10.1088/0004-637X/770/2/103](https://doi.org/10.1088/0004-637X/770/2/103)
- Hui, C. Y., & Li, K. L. 2019, *Galaxies*, 7, doi: [10.3390/galaxies7040093](https://doi.org/10.3390/galaxies7040093)
- Kandel, D., Romani, R. W., & An, H. 2019, *ApJ*, 879, 73, doi: [10.3847/1538-4357/ab24d9](https://doi.org/10.3847/1538-4357/ab24d9)
- Kudale, S., Roy, J., Bhattacharyya, B., Stappers, B., & Chengalur, J. 2020, *ApJ*, 900, 194, doi: [10.3847/1538-4357/aba902](https://doi.org/10.3847/1538-4357/aba902)
- Lebofsky, M., Croft, S., Siemion, A. P. V., et al. 2019, *PASP*, 131, 124505, doi: [10.1088/1538-3873/ab3e82](https://doi.org/10.1088/1538-3873/ab3e82)
- Li, K.-L., Kong, A. K. H., Hou, X., et al. 2016, *The Astrophysical Journal*, 833, 143, doi: [10.3847/1538-4357/833/2/143](https://doi.org/10.3847/1538-4357/833/2/143)
- Li, M., Halpern, J. P., & Thorstensen, J. R. 2014, *The Astrophysical Journal*, 795, 115, doi: [10.1088/0004-637x/795/2/115](https://doi.org/10.1088/0004-637x/795/2/115)
- Linares, M. 2014, *ApJ*, 795, 72, doi: [10.1088/0004-637X/795/1/72](https://doi.org/10.1088/0004-637X/795/1/72)
- Linares, M., Miles-Páez, P., Rodríguez-Gil, P., et al. 2017, *MNRAS*, 465, 4602, doi: [10.1093/mnras/stw3057](https://doi.org/10.1093/mnras/stw3057)
- Lorimer, D. R., & Kramer, M. 2004, *Handbook of Pulsar Astronomy*, Vol. 4 (Cambridge: Cambridge Univ. Press)
- Lynch, R. S. 2012, *Proceedings of the International Astronomical Union*, 8, 41, doi: [10.1017/s1743921312023113](https://doi.org/10.1017/s1743921312023113)
- MacMahon, D. H. E., Price, D. C., Lebofsky, M., et al. 2018, *PASP*, 130, 044502, doi: [10.1088/1538-3873/aa80d2](https://doi.org/10.1088/1538-3873/aa80d2)
- Masci, F. J., Laher, R. R., Rusholme, B., et al. 2018, *Publications of the Astronomical Society of the Pacific*, 131, 018003, doi: [10.1088/1538-3873/aae8ac](https://doi.org/10.1088/1538-3873/aae8ac)
- Mirabal, N., Charles, E., Ferrara, E. C., et al. 2016, *The Astrophysical Journal*, 825, 69, doi: [10.3847/0004-637x/825/1/69](https://doi.org/10.3847/0004-637x/825/1/69)
- Morris, S. L., & Naftilan, S. A. 1993, *ApJ*, 419, 344, doi: [10.1086/173488](https://doi.org/10.1086/173488)
- NASA High Energy Astrophysics Science Archive Research Center (Heasarc). 2014, HEASoft: Unified Release of FTOOLS and XANADU, Astrophysics Source Code Library, record ascl:1408.004. <http://ascl.net/1408.004>
- Nice, D. J., & Thorsett, S. E. 1992, *ApJ*, 397, 249, doi: [10.1086/171784](https://doi.org/10.1086/171784)
- Papitto, A., & de Martino, D. 2020, arXiv e-prints, arXiv:2010.09060. <https://arxiv.org/abs/2010.09060>
- Papitto, A., Ferrigno, C., Bozzo, E., et al. 2013, *Nature*, 501, 517, doi: [10.1038/nature12470](https://doi.org/10.1038/nature12470)
- Polzin, E. J., Breton, R. P., Bhattacharyya, B., et al. 2020, *MNRAS*, 494, 2948, doi: [10.1093/mnras/staa596](https://doi.org/10.1093/mnras/staa596)
- Polzin, E. J., Breton, R. P., Clarke, A. O., et al. 2018, *MNRAS*, 476, 1968, doi: [10.1093/mnras/sty349](https://doi.org/10.1093/mnras/sty349)
- Price, D. C., Flynn, C., & Deller, A. 2021, *PASA*, 38, e038, doi: [10.1017/pasa.2021.33](https://doi.org/10.1017/pasa.2021.33)
- Ransom, S. M. 2001, PhD thesis, Harvard University
- Ransom, S. M., Eikenberry, S. S., & Middleditch, J. 2002, *AJ*, 124, 1788, doi: [10.1086/342285](https://doi.org/10.1086/342285)
- Ransom, S. M., Hessels, J. W. T., Stairs, I. H., et al. 2005, *Science*, 307, 892, doi: [10.1126/science.1108632](https://doi.org/10.1126/science.1108632)
- Ray, P. S., Nieder, L., Clark, C. J., et al. 2022, *ApJ*, 927, 216, doi: [10.3847/1538-4357/ac49ef](https://doi.org/10.3847/1538-4357/ac49ef)
- Roberts, M. S. E. 2013, in *Neutron Stars and Pulsars: Challenges and Opportunities after 80 years*, ed. J. van Leeuwen, Vol. 291, 127–132, doi: [10.1017/S174392131202337X](https://doi.org/10.1017/S174392131202337X)
- Romani, R. W., & Sanchez, N. 2016, *ApJ*, 828, 7, doi: [10.3847/0004-637X/828/1/7](https://doi.org/10.3847/0004-637X/828/1/7)
- Roy, J., Bhattacharyya, B., & Ray, P. S. 2014, *The Astronomer's Telegram*, 5890, 1



- Saz Parkinson, P. M., Xu, H., Yu, P. L. H., et al. 2016, *ApJ*, 820, 8, doi: [10.3847/0004-637X/820/1/8](https://doi.org/10.3847/0004-637X/820/1/8)
- Shahbaz, T., Linares, M., & Breton, R. P. 2017, *MNRAS*, 472, 4287, doi: [10.1093/mnras/stx2195](https://doi.org/10.1093/mnras/stx2195)
- Siegel, M. H., Porterfield, B. L., Linevsky, J. S., et al. 2014, *AJ*, 148, 131, doi: [10.1088/0004-6256/148/6/131](https://doi.org/10.1088/0004-6256/148/6/131)
- Stappers, B. W., Archibald, A. M., Hessels, J. W. T., et al. 2014, *The Astrophysical Journal*, 790, 39, doi: [10.1088/0004-637x/790/1/39](https://doi.org/10.1088/0004-637x/790/1/39)
- Strader, J., Swihart, S., Chomiuk, L., et al. 2019, *The Astrophysical Journal*, 872, 42, doi: [10.3847/1538-4357/aafbaa](https://doi.org/10.3847/1538-4357/aafbaa)
- Tavani, M., & Brookshaw, L. 1991, *ApJL*, 381, L21, doi: [10.1086/186187](https://doi.org/10.1086/186187)
- . 1993, *A&A*, 267, L1
- Thompson, C., Blandford, R. D., Evans, C. R., & Phinney, E. S. 1994, *ApJ*, 422, 304, doi: [10.1086/173728](https://doi.org/10.1086/173728)
- van der Merwe, C. J. T., Wadiasingh, Z., Venter, C., Harding, A. K., & Baring, M. G. 2020, *ApJ*, 904, 91, doi: [10.3847/1538-4357/abdbfb](https://doi.org/10.3847/1538-4357/abdbfb)
- van Staden, A. D., & Antoniadis, J. 2016, *ApJL*, 833, L12, doi: [10.3847/2041-8213/833/1/L12](https://doi.org/10.3847/2041-8213/833/1/L12)
- van Straten, W., & Bailes, M. 2011, *PASA*, 28, 1, doi: [10.1071/AS10021](https://doi.org/10.1071/AS10021)
- Wadiasingh, Z., Harding, A. K., Venter, C., Böttcher, M., & Baring, M. G. 2017, *ApJ*, 839, 80, doi: [10.3847/1538-4357/aa69bf](https://doi.org/10.3847/1538-4357/aa69bf)
- Wilms, J., Allen, A., & McCray, R. 2000, *ApJ*, 542, 914, doi: [10.1086/317016](https://doi.org/10.1086/317016)
- Yao, J. M., Manchester, R. N., & Wang, N. 2017, *The Astrophysical Journal*, 835, 29, doi: [10.3847/1538-4357/835/1/29](https://doi.org/10.3847/1538-4357/835/1/29)
- Zhang, L., Ridolfi, A., Blumer, H., et al. 2022, *ApJL*, 934, L21, doi: [10.3847/2041-8213/ac81c3](https://doi.org/10.3847/2041-8213/ac81c3)

## APPENDIX

We present a log of X-ray observations of 3FGL J0212.1+5320 in Table 4 and the Swift UVOT exposures in Table 5. In Figure 8, we show the long term Swift UVOT, Swift XRT (0.3–10 keV), and Fermi LAT (0.1–200 GeV) light curves. The latter was produced using the Fermitools software package from aperture photometry on data obtained from the Fermi Science Support Center<sup>5</sup> and binned in 60 day intervals.

**Table 4.** Log of NuSTAR, Chandra, and Swift XRT Observations

Telescope	ObsID	Date	Time	Exposure	Mean Count Rate <sup>a</sup>
		(UT)	(UTC)	(s)	(s <sup>-1</sup> )
NuSTAR	30601011	2020 Oct 5–7	16:46:09–15:41:09	81,737	–
Chandra	14814	2013 Aug 22	04:58:55–13:55:28	30,119	–
Swift	00041276001	2010 Oct 9	13:32–21:47	3291	$(1.5 \pm 0.2) \times 10^{-2}$
Swift	00041276002	2010 Oct 12	15:20–15:41	1238	$(0.77 \pm 0.3) \times 10^{-2}$
Swift	00088697001	2019 Apr 2	22:34–22:56	1286	$(2.3 \pm 0.5) \times 10^{-2}$
Swift	00088697003	2019 Apr 3	12:55–14:36	1926	$(0.91 \pm 0.2) \times 10^{-2}$
Swift	00089046001	2020 Oct 5	17:00–17:28	1649	$(1.2 \pm 0.3) \times 10^{-2}$
Swift	00089046002	2020 Oct 7	02:27–02:55	1670	$(2.0 \pm 0.5) \times 10^{-2}$
Swift	00095748002	2020 Dec 6–7	07:50–03:09	821	$(1.0 \pm 0.3) \times 10^{-2}$
Swift	00095748004	2020 Dec 13	06:54–07:08	832	$(0.84 \pm 0.4) \times 10^{-2}$
Swift	00095748005	2020 Dec 16	06:43–07:02	1108	$(2.9 \pm 0.7) \times 10^{-2}$
Swift	00095748006	2021 Feb 27	01:10–01:26	960	$(0.83 \pm 0.3) \times 10^{-2}$
Swift	00095812001	2021 Nov 28	00:28–08:38	980	$(1.2 \pm 0.6) \times 10^{-2}$
Swift	00095812003	2022 Apr 9	21:01–21:15	847	$(1.0 \pm 0.4) \times 10^{-2}$
Swift	00096553001	2022 Jun 18	05:51–06:06	915	$(1.2 \pm 0.5) \times 10^{-2}$
Swift	00095812004	2022 Jun 26	04:25–17:32	1427	$(1.6 \pm 0.4) \times 10^{-2}$
Swift	00096553002	2022 Sep 10	22:00–22:15	920	$(0.80 \pm 0.3) \times 10^{-2}$
Swift	00096553003	2022 Dec 3	08:25–11:52	1121	$(1.4 \pm 0.4) \times 10^{-2}$

<sup>a</sup>Due to the Swift coverage being sparse, we calculated only the mean net count rate (0.3–10 keV) per observation, as described in Section 6.2.

<sup>5</sup> See <https://fermi.gsfc.nasa.gov/ssc/data/access/> for details.

**Table 5.** Log of Swift UVOT Photometry

ObsID	Date (UT)	Time <sup>a</sup> (MJD UTC)	Magnitude			
			<i>U</i>	<i>UVW1</i>	<i>UVM2</i>	<i>UVW2</i>
00041276001	2010 Oct 9	55478.5683	...	...	19.84(09)	...
		55478.6350	...	...	19.57(07)	...
		55478.7040	...	...	19.43(09)	...
		55478.7707	...	...	19.58(09)	...
		55478.8383	...	...	19.73(12)	...
		55478.9053	...	...	19.73(11)	...
00041276002	2010 Oct 12	55481.6463	...	...	...	19.72(05)
00088697001	2019 April 2	58575.9479	...	17.98(03)	...	...
00088697003	2019 April 3	58576.5478	16.22(02)	...	...	...
		58576.6066	16.21(03)	...	...	...
00089046001	2020 Oct 5	59127.7179	...	17.73(03)	...	...
00089046002	2020 Oct 7	59129.1116	...	...	...	19.16(05)
00095748002	2020 Dec 6–7	59189.3264	...	...	...	19.25(22)
		59189.3360	...	...	...	19.01(07)
		59190.1299	...	...	19.53(19)	...
00095748004	2020 Dec 13	59196.2921	16.26(03)	...	...	...
00095748005	2020 Dec 16	59199.2864	16.21(03)	...	...	...
00095748006	2021 Feb 27	59272.0539	16.28(03)	...	...	...
00095812001	2021 Nov 28	59546.0239	...	...	19.28(09)	...
		59546.3580	...	...	19.28(15)	...
00095812003	2022 April 9	59678.8802	...	...	19.13(08)	...
00096553001	2022 June 18	59748.2486	16.23(03)	...	...	...
00095812004	2022 June 26	59756.1886	16.10(03)	...	...	...
		59756.7268	16.23(03)	...	...	...
00096553002	2022 Sep 10	59832.9214	16.32(03)	...	...	...
00096553003	2022 Dec 3	59916.3518	16.31(03)	...	...	...
		59916.4890	16.20(03)	...	...	...

<sup>a</sup>Mid-time of the exposure.

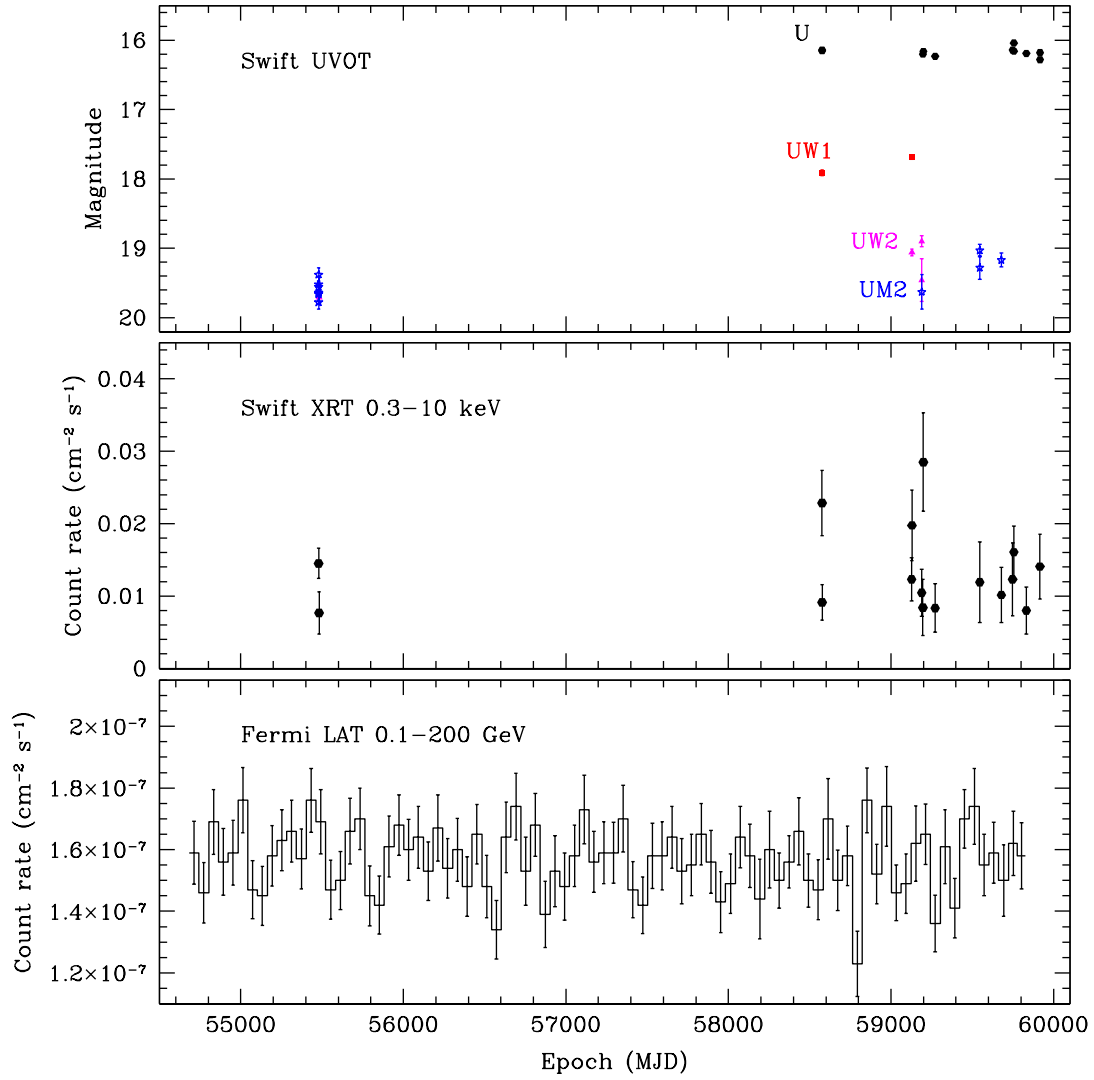


**Figure 8.** Long term light curves of 3FGL J0212.1+5320 from Swift UVOT and XRT (0.3–10 keV), and Fermi LAT (0.1–200 GeV) exposure-corrected aperture photometry light curve binned at 60 days. The Swift UVOT data include filters *UVM2* (blue), *UVW2* (magenta), *UVW1* (red), and *U* (black).